GEOPHYSICS, VOL. 86, NO. 3 (MAY-JUNE 2021); P. T155–T164, 11 FIGS.
10.1190/GEO2020-0515.1

Simulation of thermoelastic waves based on the Lord-Shulman theory

Wanting Hou[1], Li-Yun Fu[2], José M. Carcione[3], Zhiwei Wang[1], and Jia Wei[4]

ABSTRACT

Thermoelasticity is important in seismic propagation due to the effects related to wave attenuation and velocity dispersion. We have applied a novel finite-difference (FD) solver of the Lord-Shulman thermoelasticity equations to compute synthetic seismograms that include the effects of the thermal properties (expansion coefficient, thermal conductivity, and specific heat) compared with the classic forward-modeling codes. We use a time splitting method because the presence of a slow quasistatic mode (the thermal mode) makes the differential equations stiff and unstable for explicit time-stepping methods. The spatial derivatives are computed with a rotated staggered-grid FD method, and an unsplit convolutional perfectly matched layer is used to absorb the waves at the boundaries, with an optimal performance at the grazing incidence. The stability condition of the modeling algorithm is examined. The numerical experiments illustrate the effects of the thermoelasticity properties on the attenuation of the fast P-wave (or E-wave) and the slow thermal P-wave (or T-wave). These propagation modes have characteristics similar to the fast and slow P-waves of poroelasticity, respectively. The thermal expansion coefficient has a significant effect on the velocity dispersion and attenuation of the elastic waves, and the thermal conductivity affects the relaxation time of the thermal diffusion process, with the T mode becoming wave-like at high thermal conductivities and high frequencies.

INTRODUCTION

The theory of thermoelasticity describes the coupling between elastic deformation and temperature, based on the classic theory of elasticity and the heat-conduction equation. The theory has been considered in earthquake seismology (Boschi, 1973), geothermal exploration (Jacquey et al., 2015), and in the exploration of high-pressure, high-temperature deep reservoirs of hydrocarbon source rocks (Fu, 2012, 2017). The classic theory has been established by Biot (1956a) based on a parabolic equation of heat conduction. However, this theory predicts infinite velocities. The Lord-Shulman (LS) model overcomes this problem (Lord and Shulman, 1967) by transforming the heat equation into a hyperbolic one, including a relaxation time. The theory predicts an additional P-wave called the thermal wave (T-wave) having characteristics similar to the slow P-wave of poroelasticity (Biot, 1956b). The existence of the T-wave has been verified in experimental measurements in solid helium (Ackerman et al., 1966) and sodium fluoride (NaF) crystals (Jackson et al., 1970; McNelly et al., 1970).

Numerical simulation of seismic wave propagation is an important tool for studying geophysical exploration such as geothermal exploration and earthquake seismology. Including thermal effects is important for modeling the effects of attenuation and velocity dispersion. Several simulation techniques are reported in the elastic case, such as the finite-difference (FD) (Zhang et al., 2014), finite-element (Serón et al., 1990), boundary elements (Fu and Mou, 1994; Hu et al., 2009), and spectral (Faccioli et al., 1997) methods. In particular, Veres et al. (2013) and Carcione et al. (2019a, 2019b) include LS thermoelasticity effects, based on staggered FD grids and the Fourier pseudospectral method, respectively. Moreover, Green's functions are available (Wang et al., 2020; Wei et al.,

Manuscript received by the Editor 17 July 2020; revised manuscript received 22 December 2020; published ahead of production 1 February 2021; published online 08 April 2021.
[1]China University of Petroleum (East China), Key Laboratory of Deep Oil and Gas, 66 Changjiang West Road, Huangdao District, Qingdao 266580, China. E-mail: hwtupc@163.com; wzw@mail.iggcas.ac.cn.
[2]China University of Petroleum (East China), Key Laboratory of Deep Oil and Gas, 66 Changjiang West Road, Huangdao District, Qingdao 266580, China and Qingdao National Laboratory for Marine Science and Technology, Laboratory for Marine Mineral Resources, Qingdao 266071, China. E-mail: lfu@upc.edu.cn (corresponding author).
[3]Istituto Nazionale di Oceanografia e di Geofisica Sperimentale (OGS), Borgo Grotta Gigante 42c, Sgonico, Trieste 34010, Italy and Hohai University, School of Earth Sciences and Engineering, Nanjing 210098, China. E-mail: jose.carcione@gmail.com.
[4]Chinese Academy of Sciences, Institute of Geology and Geophysics, 19 Beitucheng Western Road, Chaoyang District, Beijing 100029, China. E-mail: jiawei@mail.iggcas.ac.cn.

2020). Shaw and Mukhopadhyay (2011) study thermoelastic waves with thermal relaxation in an isotropic micropolar plate.

Staggered grids can effectively improve the accuracy of FD methods and are widely used in numerical simulations. However, in the presence of strong heterogeneities, standard staggered grids (SSGs) cause instabilities and boundary problems (Virieux, 1986). Here, we use rotated staggered grids (RSGs) (Saenger et al., 2000; Saenger and Shapiro, 2002), which can handle these problems, even for high-contrast discontinuities. Moreover, we implement effective absorbing boundaries based on the unsplit convolutional perfectly matched layer (CPML) method, which requires limited memory storage, has good computational efficiency, and removes spurious modes at the grazing incidence and low-frequency energy (Komatitsch and Martin, 2007; Martin and Komatitsch, 2009; Wang et al., 2019). The equations, being numerically stiff, are integrated in time with a time splitting or partition method (Carcione and Quiroga-Goode, 1995).

The effect of thermal properties (specific heat, thermal conductivity, and coefficient of thermal expansion) on wave velocity and attenuation are studied with a plane-wave analysis. We first compute snapshots in a 2D homogeneous medium and a heat source, and we analyze the physics of propagation. Finally, we consider heterogeneous models consisting of layers and volcanoes.

THEORY OF THERMOELASTICITY

Biot (1956a) establishes the classic theory of thermoelasticity, in which a parabolic equation of the heat conduction equation leads to unphysical solutions, such as unrealistic infinite velocities as a function of frequency. Introducing a relaxation time into the classic equations, Lord and Shulman (1967) obtain a hyperbolic heat equation that overcomes this problem. It is worth mentioning that there are two theories of hyperbolic thermoelasticity (Ignaczak and Ostoja-Starzewski, 2010), namely, the LS model with one relaxation time and the Green-Lindsay model (Green and Lindsay, 1972) with two relaxation times. The latter is a generalization by including another (phenomenological) relaxation time in the coupling term of stress-strain relations.

The following heat equation relates the strain ϵ and temperature T as

$$\kappa\Delta T = c(\dot{T} + \tau\ddot{T}) + \gamma T_0(\dot{\epsilon} + \tau\ddot{\epsilon}) + q, \tag{1}$$

where τ is the relaxation time, κ is the thermal conductivity, c is the specific heat of the unit volume in the absence of deformation, T_0 is the reference absolute temperature, γ is the thermal modulus, q is the external heat flux, Δ is the Laplacian operator, and the dot above a variable denotes the time differentiation. The thermal modulus is related to the Lamé constants λ and μ through the linear thermal expansion coefficient α_T as

$$\gamma = (3\lambda + 2\mu)\alpha_T. \tag{2}$$

The relaxation time represents the time lag to establish a steady-state heat conduction in an element of volume when a temperature gradient is suddenly imposed on the element. As formulated in the poroelasticity theory, which introduces fluid properties to stress-strain relationships, thermoelasticity considers a temperature into it for coupling. Therefore, the relaxation time relevant to thermal properties in elastic media can be expressed as (Rudgers, 1990)

$$\tau = \frac{\kappa\rho}{c(\lambda + 2\mu)}, \tag{3}$$

where ρ is the mass density. The classic theory of thermoelasticity neglects the time lag. If the medium is subjected to a mechanical or thermal perturbation, the effects of the perturbation are felt at an infinite distance from the source. This causes unphysical behavior of thermoelastic waves propagating by an infinite velocity.

We use the Einstein implicit summation as follows. The constitutive relations for stress-strain given by Biot (1956a) are

$$\sigma_{ij} = 2\mu\epsilon_{ij} + (\lambda\epsilon - \gamma T)\delta_{ij} + f_{ij}, \tag{4}$$

where σ_{ij} and ϵ_{ij} ($i,j = x, y, z$) denote the components of the stress and strain tensors, respectively, f_{ij} is the external stress forces, δ_{ij} is the Kronecker-delta components, and $\epsilon(= \epsilon_{ii})$ is the bulk strain, with

$$2\epsilon_{ij} = u_{i,j} + u_{j,i}, \tag{5}$$

where u_i denotes the components of the displacement field and subscript ",i" denotes a spatial derivative. The equations of momentum conservation are

$$\sigma_{ij,j} = \rho\ddot{u}_i + f_i, \tag{6}$$

where f_i denotes the components of the external body force. Thus, using the strain-displacement relations (equation 5) and substituting the constitutive relations (equation 4) into the momentum equations (equation 6), we obtain the equations coupling the elastic and temperature fields,

$$\begin{aligned} &(\lambda + \mu)u_{j,ji} + \mu u_{i,jj} - \gamma T_{,i} - \rho\ddot{u}_i = 0, \\ &\kappa T_{,jj} - c(\dot{T} + \tau\ddot{T}) - \gamma T_0(\dot{u}_{j,j} + \tau\ddot{u}_{j,j}) - q = 0. \end{aligned} \tag{7}$$

Unlike classic thermoelasticity, equation 7 couples mechanical motions and time-relaxation thermal perturbations, implying the propagation of finite-velocity signals. In fact, equation 7 for the coupling of strains and temperature fields is formally analogous to the case of poroelasticity for the coupling of strains and fluid pressures (Norris, 1992). The mathematical analogy in the constitutive equations of poroelasticity and thermoelasticity implies that the elastic solid response couples with a dissipative process, namely, hydraulic and thermal conductions, respectively.

NUMERICAL METHODOLOGY

Spatial-derivative approximation and time stepping

SSG-FD methods are widely used in seismology to simulate elastic wave propagation, but RSG-FD methods achieve better performance in high-contrast heterogeneous media. The velocity components are defined in one grid, and the stress components, temperature, and physical properties are defined in another (staggered) grid (see Figure 1). Compared to the SSG-FD mesh, the RSG-FD grid consists of rhombi instead of rectangles. As indicated by Saenger et al. (2000), rotating the entire grid by 45°, the direction to derive spatial derivatives follows the diagonal of an evenly sampled mesh.

As shown in Figure 1, we rotate the direction of the spatial derivatives from the horizontal and vertical directions x and z to the diagonal directions $\tilde{x}$ and $\tilde{z}$ as

$$\begin{aligned} \tilde{\mathbf{x}} &= \frac{\Delta x}{\Delta r}\mathbf{x} - \frac{\Delta z}{\Delta r}\mathbf{z}, \\ \tilde{\mathbf{z}} &= \frac{\Delta x}{\Delta r}\mathbf{x} + \frac{\Delta z}{\Delta r}\mathbf{z}, \end{aligned} \tag{8}$$

where Δr denotes the diagonal length of the grid element $\sqrt{\Delta x^2 + \Delta z^2}$. Hence, the spatial derivatives along the new diagonal directions are

$$\frac{\partial}{\partial x} = \frac{\Delta r}{2\Delta x}\left(\frac{\partial}{\partial \tilde{z}} + \frac{\partial}{\partial \tilde{x}}\right),$$
$$\frac{\partial}{\partial z} = \frac{\Delta r}{2\Delta z}\left(\frac{\partial}{\partial \tilde{z}} - \frac{\partial}{\partial \tilde{x}}\right). \tag{9}$$

Analogous to equation 9, the $2N$th-order derivatives are shown in equation A-1. The first-order velocity-stress-temperature formulation of the 2D thermoelasticity equations is implemented from equations 1 to 6 as

$$\begin{aligned}
\dot{V}_x &= \rho^{-1}(\partial_x \sigma_{xx} + \partial_z \sigma_{xz} - f_x),\\
\dot{V}_z &= \rho^{-1}(\partial_x \sigma_{xz} + \partial_z \sigma_{zz} - f_z),\\
\dot{\sigma}_{xx} &= (\lambda + 2\mu)\partial_x V_x + \lambda \partial_z V_z - \gamma\phi + \dot{f}_{xx},\\
\dot{\sigma}_{zz} &= (\lambda + 2\mu)\partial_z V_z + \lambda \partial_x V_x - \gamma\phi + \dot{f}_{zz},\\
\dot{\sigma}_{xz} &= \mu(\partial_z V_x + \partial_x V_z) + \dot{f}_{xz},\\
\dot{T} &= \phi,\\
\dot{\phi} &= -\frac{\gamma T_0}{c\tau}(\partial_x V_x + \partial_z V_z) - \frac{\gamma T_0}{c\rho}(\partial_{xx}\sigma_{xx} + \partial_{zz}\sigma_{zz} + 2\partial_{xz}\sigma_{xz})\\
&\quad + \frac{\kappa}{c\tau}(\partial_{xx} T + \partial_{zz} T) - \frac{1}{\tau}\phi - q',
\end{aligned} \tag{10}$$

where $q' = (q/c\tau) - (\gamma T_0/c\rho)(f_{x,x} + f_{z,z})$. This set of equations can be combined into a matrix system as

$$\dot{\mathbf{v}} + \mathbf{s} = \mathbf{M}\mathbf{v}, \tag{11}$$

where the 7×7 matrix $\mathbf{Mv}$ is given by

$$\mathbf{Mv} = \begin{bmatrix}
0 & 0 & \frac{\partial_x}{\rho} & 0 & \frac{\partial_z}{\rho} & 0 & 0\\
0 & 0 & 0 & \frac{\partial_z}{\rho} & \frac{\partial_x}{\rho} & 0 & 0\\
(\lambda+2\mu)\partial_x & \lambda\partial_z & 0 & 0 & 0 & 0 & -\gamma\\
\lambda\partial_x & (\lambda+2\mu)\partial_z & 0 & 0 & 0 & 0 & -\gamma\\
\mu\partial_z & \mu\partial_x & 0 & 0 & 0 & 0 & 0\\
0 & 0 & 0 & 0 & 0 & 0 & 1\\
-\frac{\gamma T_0}{c\tau}\partial_x & -\frac{\gamma T_0}{c\tau}\partial_z & -\frac{\gamma T_0}{c\rho}\partial_{xx} & -\frac{\gamma T_0}{c\rho}\partial_{zz} & -2\frac{\gamma T_0}{c\rho}\partial_{xz} & \frac{\kappa}{c\tau}(\partial_{xx}+\partial_{zz}) & -\frac{1}{\tau}
\end{bmatrix}
\times \begin{bmatrix} V_x \\ V_z \\ \sigma_{xx} \\ \sigma_{zz} \\ \sigma_{xz} \\ T \\ \phi \end{bmatrix}, \tag{12}$$

and the source vector is

$$\mathbf{s} = [\, f_x/\rho \quad f_z/\rho \quad -\dot{f}_{xx} \quad -\dot{f}_{zz} \quad -\dot{f}_{xz} \quad 0 \quad q' \,]^{\top}. \tag{13}$$

Then, we illustrate the partition method of Carcione and Quiroga-Goode (1995) to perform the time stepping. In this algorithm, equation 11 is solved in two steps. First, the matrix operator $\mathbf{M}$ is partitioned as

$$\mathbf{M} = \mathbf{M}_r + \mathbf{M}_s, \tag{14}$$

where

$$\mathbf{M}_s = \begin{bmatrix}
0 & 0 & 0 & 0 & 0 & 0 & 0\\
0 & 0 & 0 & 0 & 0 & 0 & 0\\
0 & 0 & 0 & 0 & 0 & 0 & -\gamma\\
0 & 0 & 0 & 0 & 0 & 0 & -\gamma\\
0 & 0 & 0 & 0 & 0 & 0 & 0\\
0 & 0 & 0 & 0 & 0 & 0 & 0\\
0 & 0 & 0 & 0 & 0 & 0 & -\frac{1}{\tau}
\end{bmatrix}, \tag{15}$$

and the time integration from t to $t + dt$ for this matrix is solved analytically to obtain the intermediate solutions

$$\begin{aligned}
(\sigma_{xx}^{n+1})^* &= \sigma_{xx}^n + \tau\gamma(e^{-\frac{\Delta t}{\tau}} - 1)\phi^n,\\
(\sigma_{zz}^{n+1})^* &= \sigma_{zz}^n + \tau\gamma(e^{-\frac{\Delta t}{\tau}} - 1)\phi^n,\\
(\phi^{n+1})^* &= e^{-\frac{\Delta t}{\tau}}\phi^n.
\end{aligned} \tag{16}$$

For time stepping, we use the time-splitting algorithm of Carcione et al. (2019b). Discretizing time as $t = ndt$, where dt is the time step, we have

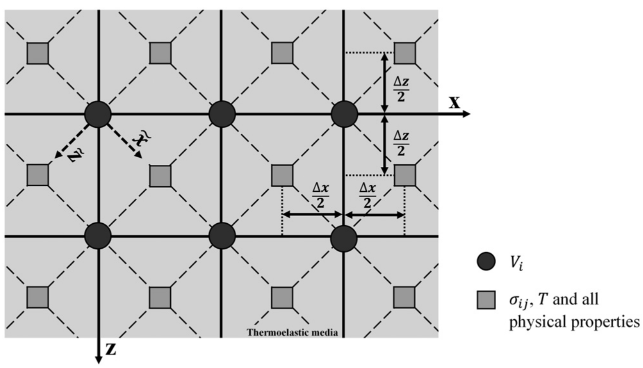

Figure 1. The RSG for the discretization of the thermoelasticity equations. The temperature T and stress components σ_{ij} are discretized on the same grid. The sizes of the rectangular elementary cells of the grid are Δx and Δz, and the diagonal directions $\tilde{x}$ and $\tilde{z}$ are obtained by rotating the horizontal and vertical directions x and z. The grid of the velocity components V_i is shifted by a half grid in both directions, i.e., $\Delta x/2$ and $\Delta z/2$.

$$
\begin{aligned}
V_x^{n+1} &= V_x^n + dt[\partial_x(\sigma_{xx}^{n+1})^* + \partial_z\sigma_{xz}^n]/\rho,\\
V_z^{n+1} &= V_z^n + dt[\partial_z(\sigma_{zz}^{n+1})^* + \partial_x\sigma_{xz}^n]/\rho,\\
\sigma_{xx}^{n+1} &= (\sigma_{xx}^{n+1})^* + dt[(\lambda+2\mu)\partial_x V_x^n + \lambda\partial_z V_z^n],\\
\sigma_{zz}^{n+1} &= (\sigma_{zz}^{n+1})^* + dt[(\lambda+2\mu)\partial_z V_z^n + \lambda\partial_x V_x^n],\\
\sigma_{xz}^{n+1} &= \sigma_{xz}^n + dt\cdot\mu(\partial_z V_x^n + \partial_x V_z^n),\\
T^{n+1} &= T^n + dt(\phi^{n+1})^*,\\
\phi^{n+1} &= (\phi^{n+1})^* + \frac{dt}{c\tau}[\kappa(\partial_{xx}+\partial_{zz})T^n - \gamma T_0(\partial_x+\partial_z)V_x^n\\
&- \frac{\tau\gamma T_0}{\rho}(\partial_{xx}(\sigma_{xx}^{n+1})^* + \partial_{zz}(\sigma_{zz}^{n+1})^* + 2\partial_{xz}\sigma_{xz}^n)],
\end{aligned}
\tag{17}
$$

where the eighth- and second-order FD approximations are used for the space and time derivatives, respectively. The variables indicated with an asterisk correspond to the intermediate solutions at each time step, as illustrated in equation 16.

Absorbing boundaries

The modeling method requires efficient absorbing boundaries to avoid unphysical reflections. The PML is a suitable technique for all incidence angles, in particular the computationally efficient unsplit CPML, illustrated in Appendix B. The algorithm is developed by modifying the complex coefficient s_x and introducing the auxiliary variables d_x, α_x, and χ_x, where d_x denotes the damping profile and $\chi_x \geq 1$ and $\alpha_x \geq 0$ are the two real variables. From equation B-2, we obtain

$$
\partial_{\tilde{x}} = \frac{1}{s_x}\partial_x = \left[\frac{1}{\chi_x} - \frac{d_x}{\chi_x^2(i\omega+\alpha_x+\frac{d_x}{\chi_x})}\right]\partial_x = \frac{1}{\chi_x}\partial_x + \tilde{\psi}_x, \tag{18}
$$

where $i=\sqrt{-1}$. The specific derivation and detailed implementation of this equation are given in Appendix B. Let ψ_x denote the inverse of $\tilde{\psi}_x$; the iterative solution of ψ_x is shown in equation B-6. We obtain

$$
\partial_{\tilde{x}} = \frac{1}{\chi_x}\partial_x + \psi_x. \tag{19}
$$

Then, applying an RSG-FD scheme with a CPML absorbing boundary to the velocity-stress-temperature equations, we obtain the final formulation of the thermoelasticity equations:

$$
\begin{aligned}
\rho\dot{V}_x &= \frac{1}{\chi_x}\partial_x\sigma_{xx} + \psi_{x,\sigma_{xx}} + \frac{1}{\chi_z}\partial_z\sigma_{xz} + \psi_{z,\sigma_{xz}},\\
\rho\dot{V}_z &= \frac{1}{\chi_x}\partial_x\sigma_{xz} + \psi_{x,\sigma_{xz}} + \frac{1}{\chi_z}\partial_z\sigma_{zz} + \psi_{z,\sigma_{zz}},\\
\dot{T} &= \phi,\\
\dot{\sigma}_{xx} &= (\lambda+2\mu)\left(\frac{1}{\chi_x}\partial_x V_x + \psi_{x,V_x}\right) + \lambda\left(\frac{1}{\chi_z}\partial_z V_z + \psi_{z,V_z}\right) - \gamma\phi,\\
\dot{\sigma}_{zz} &= (\lambda+2\mu)\left(\frac{1}{\chi_z}\partial_z V_z + \psi_{z,V_z}\right) + \lambda\left(\frac{1}{\chi_x}\partial_x V_x + \psi_{x,V_x}\right) - \gamma\phi,\\
\dot{\sigma}_{xz} &= \mu\left(\frac{1}{\chi_x}\partial_x V_z + \psi_{x,V_z} + \frac{1}{\chi_z}\partial_z V_x + \psi_{z,V_x}\right).
\end{aligned}
\tag{20}
$$

DISPERSION, ATTENUATION, AND NUMERICAL STABILITY

Velocity dispersion and attenuation

The phase velocity V_p and attenuation factor A of the two longitudinal waves are computed from the complex velocity V_c obtained in Appendix C as

$$
V_p = \left[\mathrm{Re}\left(\frac{1}{V_c}\right)\right]^{-1}, \qquad A = -\omega\,\mathrm{Im}\left(\frac{1}{V_c}\right). \tag{21}
$$

Deresiewicz (1957) introduces an attenuation coefficient, which is

$$
L = 4\pi\frac{AV_p}{\omega}. \tag{22}
$$

Stability analysis

Numerical stability is required to obtain the solution. For the velocity-stress-temperature FD equations, second order in time and $2N$th order in space, the stability condition of the rotated and classic staggered methods is

$$
V_E\cdot\Delta t\sqrt{\frac{1}{\Delta x^2}+\frac{1}{\Delta z^2}} \leq \frac{1}{C}, \tag{23}
$$

with

$$
C = \sum_{i=0}^{N}|c_i|, \tag{24}
$$

where c_i denotes the spatial difference coefficients related to the $2N$th order of the spatial derivative and V_E is the maximum wave velocity in the medium. The coefficient of the eighth-order approximation is $C = 1.2863$.

In addition to the above condition, the accuracy and stability of the RSG-FD method are dictated by the number of grid points per minimum wavelength. In general, for the eighth-order RSG-FD (Chen et al., 2006), it is

$$
\frac{V_T}{4f_0\Delta h} > 3, \tag{25}
$$

where f_0 denotes the source center frequency and Δh denotes the spatial discretization step, whereas V_T is calculated from equation C-6.

NUMERICAL SIMULATIONS

Influence of the thermoelasticity properties

The phase velocities and attenuation coefficients of the two longitudinal waves are calculated from their complex velocities obtained as the roots of equation C-3, whereas the shear velocity V_S is not affected in homogeneous media as shown in equation C-2.

In all of the numerical simulations, except where stated otherwise, the elastic constants are those of Carcione et al. (2019b):

$\rho = 2560$ kg/m^3, $\lambda = 4.2$ GPa, $\mu = 6.4$ GPa, $T_0 = 300$ K, $\alpha_T = 0.24 \times 10^{-6}$ K^{-1}, $\kappa = 9.5$ mkg/(s^{3}K), and $c = 146$ kg/(ms^{2}K). We vary these thermal properties (thermal conductivity, thermal expansion coefficient, and specific heat) to investigate the frequency dependence of two P-waves (P and T) and an S-wave (S). The three thermal parameters constitute the basic thermoelastic coefficients of rock materials that control the propagation characteristics of thermoelastic waves. Especially, the thermal conductivity characterizes the thermophysical property of rocks. It is the most important parameter because heat transfer in the lithosphere is controlled by heat conduction. Other thermal properties can be determined from these three basic parameters.

Figures 2, 3, and 4 show the frequency dependence of phase velocity and attenuation for the P-, T-, and S-waves. As expected, the S-wave phase velocity is independent of frequency because the shear strain is not coupled with the heat equation; that is, the S-waves are not affected by the temperature. From Figure 2, with three thermal conductivities in steps of 5 m kg/(s^3 K), we see that the relaxation peak of the P-wave moves toward the low frequencies with increasing thermal conductivity (see Figure 2a), but with the same width of the peak and maximum attenuation (see Figure 2b). The relaxation frequency is approximately $f_r = \omega_r/2\pi = 1/\tau$ (Wang and Santamarina, 2007). For the P- and T-waves, the low- and high-frequency limits do not change by varying the conductivity. Higher conductivity requires longer times or lower frequencies for the medium to relax, and this behavior can be observed in the snapshots presented subsequently.

Figure 3 illustrates the effect of different thermal expansion coefficients (varying in steps of 6×10^{-7} K^{-1}) on the frequency dependence of the phase velocity (Figure 3a) and attenuation (Figure 3b) for these waves. The thermal expansion coefficient describes temperature-induced linear or volume changes in rocks. It characterizes the magnitude of thermal expansion, associated closely to thermal stresses and strains. The results show that the relaxation frequencies move toward lower values with increasing thermal expansion coefficient, as in the case of the thermal conductivity, but in this case the shift is smaller and the attenuation values are comparable. However, the P-wave velocity increases, whereas that of the T-wave decreases for increasing thermal expansion. Figure 4 shows the results by varying the specific heat capacity in steps of 40 kg/(m s^2 K). Compared with Figure 3, the behavior is the opposite when the heat capacity increases.

The thermal mode (T-wave) has characteristics similar to the slow P-wave of poroelasticity. It is diffusive at low thermal conductivities, but it becomes wave-like for high thermal conductivities. Like the slow P-wave of poroelasticity, the T-wave is diffusive at low frequencies. The behavior depends on the thermal conductivity and specific heat as shown in equation 3, whereas it is related to the fluid viscosity and permeability ratio in Biot's case.

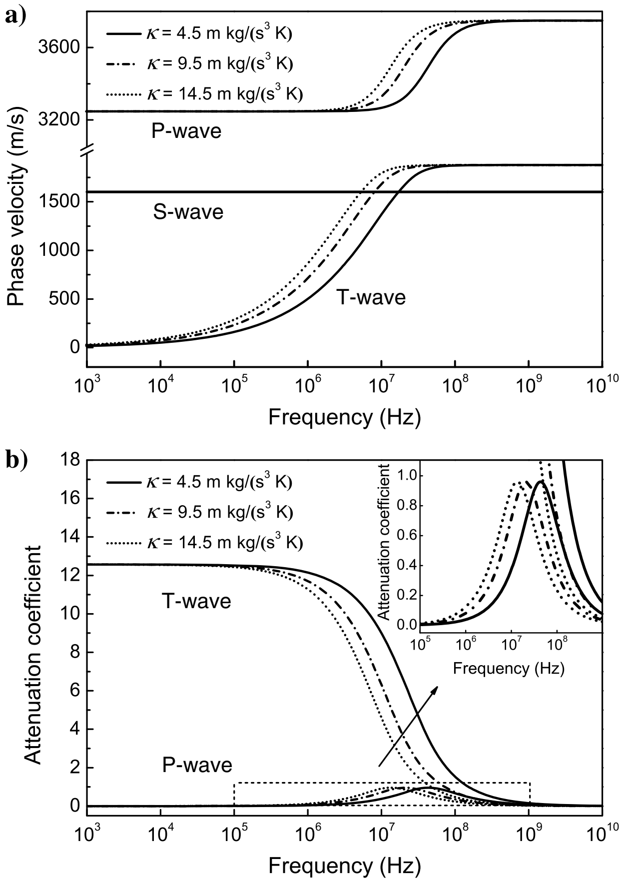

Figure 2. (a) Phase velocity and (b) attenuation coefficient of the P-, S-, and T-waves as a function of frequency, where we vary the thermal conductivity in steps of 5 m kg/(s^3 K).

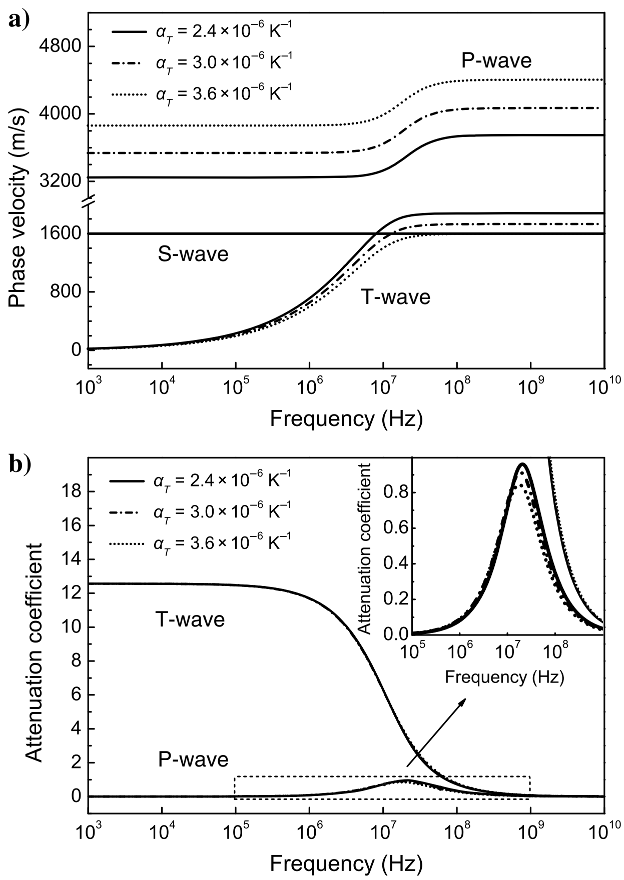

Figure 3. (a) Phase velocity and (b) attenuation coefficient of the P-, S-, and T-waves as a function of frequency, where we vary the thermal expansion coefficient in steps of 0.6×10^{-6} K^{-1}.

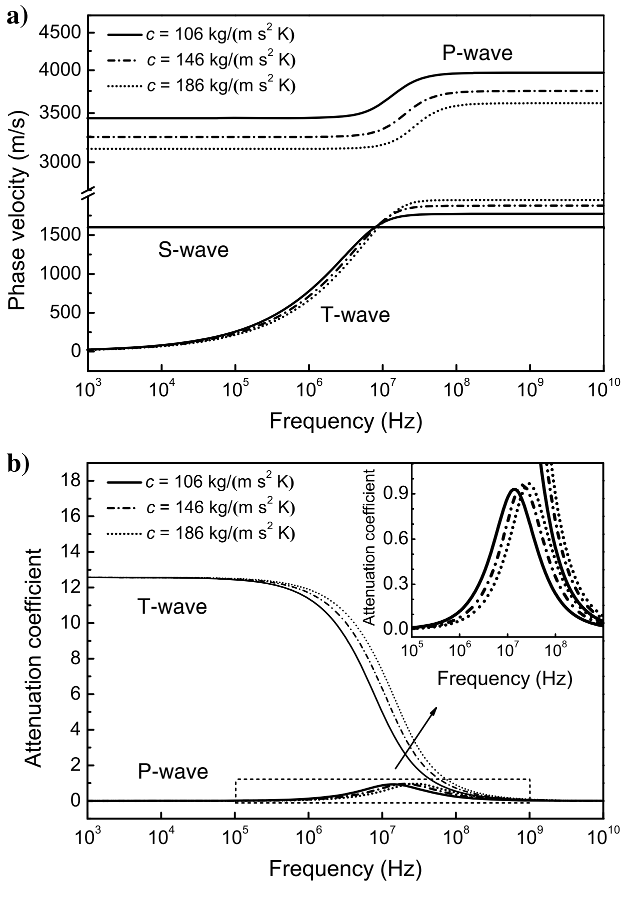

Figure 4. (a) Phase velocity and (b) attenuation coefficient of the P-, S-, and T-waves as a function of frequency, where we vary the specific heat in steps of $40\,\mathrm{kg/(m\,s^2\,K)}$.

Wave simulation in a homogeneous medium

We consider 501 grid points along the horizontal and vertical directions, with a grid size of $\Delta x = \Delta y = 0.3$ mm and $\Delta t = 10$ ns. The source is a Ricker wavelet with a dominant frequency of 0.6 MHz located at the center of the mesh [grid (251, 251)]. For comparison, snapshots of the different field variables with $\kappa = 9.5\ \mathrm{m\,kg/(s^3\,K)}$ and $\kappa = 9500\ \mathrm{m\,kg/(s^3\,K)}$ are computed at $t = 16$ μs (Figures 5 and 6, respectively). The wavefront of the E- (or P-) wave travels with the adiabatic velocity $V_A = 3247$ m/s and the high-frequency velocities are $V_{E(\omega\to\infty)} = 3749$ m/s and $V_{T(\omega\to\infty)} = 1878$ m/s. As expected, the S-wave is not present. In Figure 5, the thermal wave is diffusive, with a high value of the attenuation coefficient (see Figure 2b). On the contrary, the T-wave is wave-like in Figure 6 because of its negligible attenuation. Two longitudinal waves are coupled here. According to the stress-strain relationships, if α_T is equal to zero, the two waves become uncoupled.

CMPL absorbing boundary

Then, we compute 2D snapshots by implementing the CPML method, in which the thermal conductivity is $\kappa = 9500\ \mathrm{m\,kg/(s^3\,K)}$. The stress component σ_{zz} due to a heat source is obtained at 15 and 30 μs, and the CPML absorbing boundary has a length of 40 Δx (see Figure 7a and 7b, respectively). The source is located at grid point (400, 100), and it has a central frequency of 0.6 MHz. We can see that the spurious waves disappear at the edges of the model.

Figure 8 compares synthetic seismograms at different receiver locations, where we can see the absorption effect due to the distinct thicknesses of the absorbing boundary. For clarity, Figure 9 compares the traces at the source location, where it is evident that the T-wave is more damped; otherwise, it becomes stronger. The behavior is also associated with the thermal parameter and center frequency used for

Figure 5. Snapshots at 16 μs of the (a) stress component σ_{zz}, (b) particle-velocity component V_z, and (c) temperature field for a heat source with a center frequency of 0.6 MHz. The thermal conductivity is $\kappa = 9.5\ \mathrm{m\,kg/(s^3\,K)}$.

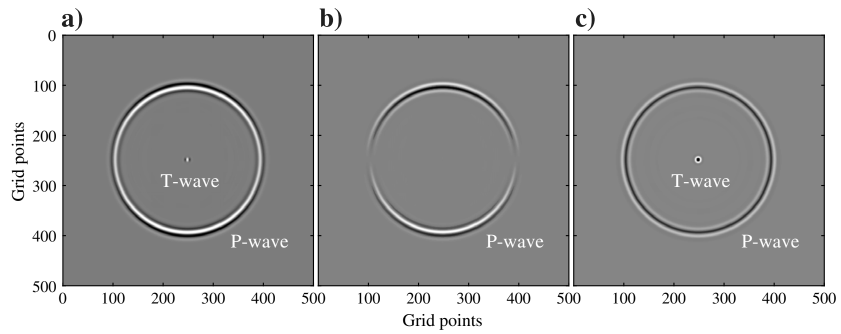

Figure 6. The remaining values are the same as in Figure 5, with $\kappa = 9500\ \mathrm{m\,kg/(s^3\,K)}$.

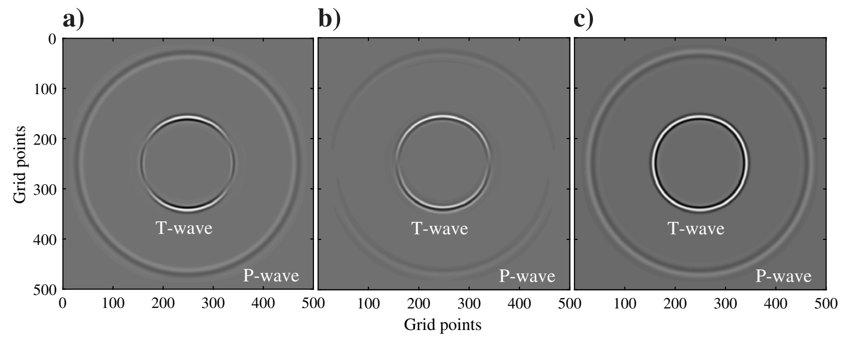

simulation. In this example, we use $\kappa = 9500\ \mathrm{m\,kg/(s^3\,K)}$ and $f_0 = 0.6$ MHz, indicating a negligible attenuation for thermal wave.

Wave simulation in an inhomogeneous medium

An inhomogeneous-layered model with two interfaces is shown in Figure 10, in which the dominant frequency is 60 Hz. We vary only the thermal conductivity, whereas the other thermoelastic properties are those of the previous section. The snapshots are computed at 0.16 s propagation time. The reflected, transmitted, and converted transmitted waves are denoted by r, t, and tc, respectively; rc is a converted reflected wave. Even if the model has two flat interfaces, the wavefield is complex, and it could be more complex in the presence of S-waves.

Finally, we compute wavefields at 0.6 s in more complex media, representing volcanoes (Figure 11), where we consider a center source frequency of $f_0 = 15$ Hz. In Figure 11a, the thermal conductivities inside and outside the volcano are $\kappa = 10^{10}\ \mathrm{m\,kg/(s^3\,K)}$ and $\kappa = 9.5\ \mathrm{m\,kg/(s^3\,K)}$, respectively. The example in Figure 11b has these values exchanged. We can see the complex seismic response generated by the volcanoes. The results indicate that the T-wave can

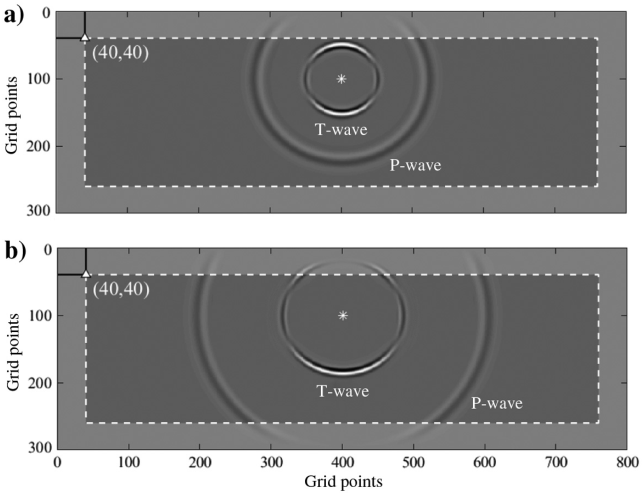

Figure 7. Snapshots at (a) $10\,\mu$s and (b) $15\,\mu$s of the σ_{zz} component due to a heat source located at grid point (400, 100). The CMPL layers of length $40\,\Delta x$ are implemented. The source center frequency is 0.6 MHz, and the thermal conductivity is $\kappa = 9500\ \mathrm{m\,kg/(s^3\,K)}$.

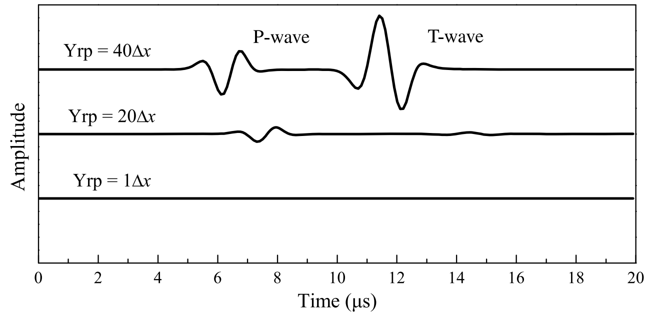

Figure 9. Comparison of the traces at the source location, corresponding to the seismograms shown in Figure 8.

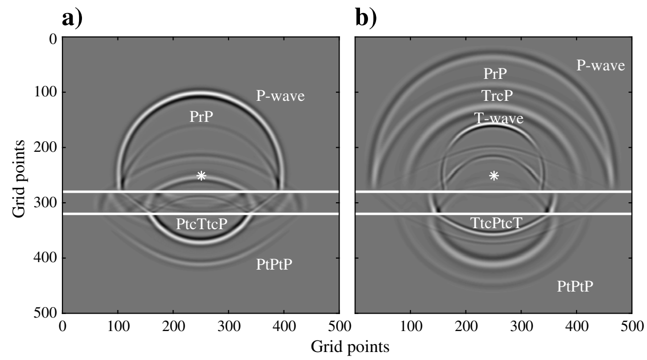

Figure 10. Snapshots at 0.16 s of the σ_{zz} component due to a heat source indicated by a star with $f_0 = 60$ Hz. (a) The upper and lower half-spaces have $\kappa = 9.5\ \mathrm{m\,kg/(s^3\,K)}$ and the layer has $\kappa = 10^{10}\ \mathrm{m\,kg/(s^3\,K)}$. (b) The snapshot after the values of thermal conductivity used in (a) are reversed. The images show the direct, reflected (r), converted (c), and transmitted (t) waves.

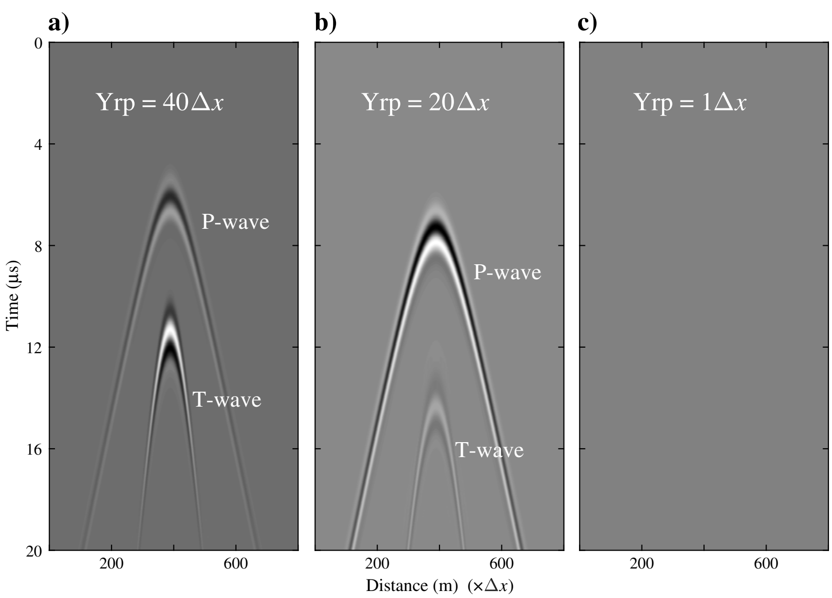

Figure 8. Synthetic seismogram using a CPML absorbing boundary of length $40\Delta x$: Yrp indicates the ordinate of the receiver position at (a) $40\,\Delta x$, (b) $20\ \Delta x$, and (c) $1\ \Delta x$, respectively.

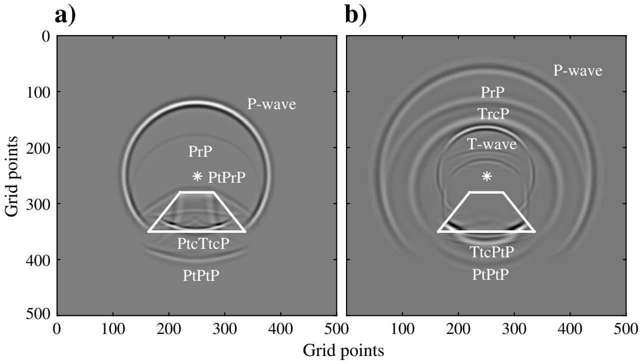

Figure 11. Snapshots at 0.6 s of the σ_{zz} component due to a heat source indicated by a star [grid point (251,251)], with $f_0 = 15$ Hz. The body is a volcano, corresponding to (a) wave-like and (b) diffusive T modes, depending on the thermal conductivity. (a) The conductivities inside and outside the volcano are $\kappa = 10^{10}\ \mathrm{m\,kg/(s^3\,K)}$ and $\kappa = 9.5\ \mathrm{m\,kg/(s^3K)}$, respectively. (b) The snapshot after the conductivity values used in (a) are reversed. The images show the direct, reflected (r), converted (c), and transmitted (t) waves.

also be used to map, when possible, the geometry of heterogeneous thermal bodies.

CONCLUSION

We apply a numerical technique to model wave propagation in a thermoelastic medium. The algorithm is based on a rotated staggered-grid FD method to compute the spatial derivatives and a partition (splitting) algorithm for time stepping. Reflections from the model boundaries are damped with an unsplit CPML absorbing method. The modeling allows us to compute snapshots of the wavefield and synthetic seismograms. A plane-wave analysis shows how the thermal properties affect the phase velocities and attenuation coefficients of the longitudinal elastic and thermal waves, indicating that introducing heat effects into the wave equation is important. The longitudinal wave generates temperature gradients leading to mechanical energy dissipation and heat-conduction absorption, whereas the heat equation predicts a T-wave analogous to the slow P-wave of the Biot theory of poroelasticity. In the low-frequency range, the thermal wave is a diffusive mode especially at low thermal conductivities, whereas it is wave-like at high frequencies. It is similar to the behavior exhibited in poroelasticity. The modeling illustrates the wavefield generated by a heat source in homogeneous and heterogeneous media, in particular, the complex wave pattern observed even in simple cases, due to the presence of the thermal wave and multiple mode conversions.

ACKNOWLEDGMENTS

This research is supported by the National Natural Science Foundation of China (Grant Nos. 41821002, 41720104006) and 111 Project "Deep-Superdeep Oil & Gas Geophysical Exploration" (B18055).

DATA AND MATERIALS AVAILABILITY

Data associated with this research are available and can be obtained by contacting the corresponding author.

APPENDIX A

COMPUTATION OF SPATIAL DERIVATIVES AND TIME STEPPING

Here, we illustrate the RSG-FD algorithm. With $2N$th-order precision, we have the $2N$th-order derivatives for velocity, stress, and temperature:

$$\begin{aligned}
\left.\frac{\partial V_i}{\partial x}\right|_{(x,z)} &= \sum_{n=1}^{N}\frac{c_n}{2\Delta x}\Bigg[V_i\Big|_{x+(n-\frac{1}{2})\Delta x,z+(n-\frac{1}{2})\Delta z} + V_i\Big|_{x+(n-\frac{1}{2})\Delta x,z-(n-\frac{1}{2})\Delta z} \\
&\quad - V_i\Big|_{x-(n-\frac{1}{2})\Delta x,z-(n-\frac{1}{2})\Delta z} - V_i\Big|_{x-(n-\frac{1}{2})\Delta x,z+(n-\frac{1}{2})\Delta z}\Bigg], \\
\left.\frac{\partial V_i}{\partial z}\right|_{(x,z)} &= \sum_{n=1}^{N}\frac{c_n}{2\Delta z}\Bigg[V_i\Big|_{x+(n-\frac{1}{2})\Delta x,z+(n-\frac{1}{2})\Delta z} - V_i\Big|_{x+(n-\frac{1}{2})\Delta x,z-(n-\frac{1}{2})\Delta z} \\
&\quad - V_i\Big|_{x-(n-\frac{1}{2})\Delta x,z-(n-\frac{1}{2})\Delta z} + V_i\Big|_{x-(n-\frac{1}{2})\Delta x,z+(n-\frac{1}{2})\Delta z}\Bigg], \\
\left.\frac{\partial \sigma_{ij}}{\partial x}\right|_{(x+\frac{1}{2},z+\frac{1}{2})} &= \sum_{n=1}^{N}\frac{c_n}{2\Delta x}\Bigg[\sigma_{ij}\Big|_{x+n\Delta x,z+n\Delta z} + \sigma_{ij}\Big|_{x+n\Delta x,z-(n-1)\Delta z} \\
&\quad - \sigma_{ij}\Big|_{x-n\Delta x,z-(n-1)\Delta z} - \sigma_{ij}\Big|_{x-n\Delta x,z+n\Delta z}\Bigg], \\
\left.\frac{\partial \sigma_{ij}}{\partial z}\right|_{(x+\frac{1}{2},z+\frac{1}{2})} &= \sum_{n=1}^{N}\frac{c_n}{2\Delta z}\Bigg[\sigma_{ij}\Big|_{x+n\Delta x,z+n\Delta z} - \sigma_{ij}\Big|_{x+n\Delta x,z-(n-1)\Delta z} \\
&\quad - \sigma_{ij}\Big|_{x-n\Delta x,z-(n-1)\Delta z} + \sigma_{ij}\Big|_{x-n\Delta x,z+n\Delta z}\Bigg], \\
\left.\frac{\partial T}{\partial x}\right|_{(x+\frac{1}{2},z+\frac{1}{2})} &= \sum_{n=1}^{N}\frac{c_n}{2\Delta x}\Bigg[T\Big|_{x+n\Delta x,z+n\Delta z} + T\Big|_{x+n\Delta x,z-(n-1)\Delta z} \\
&\quad - T\Big|_{x-n\Delta x,z-(n-1)\Delta z} - T\Big|_{x-n\Delta x,z+n\Delta z}\Bigg], \\
\left.\frac{\partial T}{\partial z}\right|_{(x+\frac{1}{2},z+\frac{1}{2})} &= \sum_{n=1}^{N}\frac{c_n}{2\Delta z}\Bigg[T\Big|_{x+n\Delta x,z+n\Delta z} - T\Big|_{x+n\Delta x,z-(n-1)\Delta z} \\
&\quad - T\Big|_{x-n\Delta x,z-(n-1)\Delta z} + T\Big|_{x-n\Delta x,z+n\Delta z}\Bigg],
\end{aligned} \tag{A-1}$$

where c_n denotes the difference coefficients.

APPENDIX B

CPMLS FOR THE THERMOELASTICITY EQUATIONS

The CPML is implemented by using complex coordinates as

$$\tilde{x} = x - \frac{i}{\omega}\int_0^x d_x(s)ds \tag{B-1}$$

and

$$\partial_{\tilde{x}} = \frac{1}{s_x}\partial_x, \tag{B-2}$$

where

$$s_x = \frac{i\omega + d_x}{i\omega} = 1 + \frac{d_x}{i\omega}. \tag{B-3}$$

The extension function is

$$s_x = \chi_x + \frac{d_x}{\alpha_x + i\omega}. \tag{B-4}$$

In equation 18, $\tilde{\psi}_x$ is written as

$$i\tilde{\omega}\tilde{\psi}_x + \left(\alpha_x + \frac{d_x}{\chi_x}\right)\tilde{\psi}_x = -\frac{d_x}{\chi_x^2}\partial_x. \tag{B-5}$$

Let ψ_x denote the inverse of $\tilde{\psi}_x$ and ψ_x is

$$\psi_x^n = \psi_x^{n-1} e^{-(\alpha_x + \frac{d_x}{\chi_x})\Delta t} + \left(e^{-(\alpha_x + \frac{d_x}{\chi_x})\Delta t} - 1\right)\frac{d_x}{\chi_x(\chi_x\alpha_x + d_x)}\partial_x, \tag{B-6}$$

and we use the damping profile

$$d_x(l) = d_{\max}\left(\frac{l}{L}\right)^m, \tag{B-7}$$

with

$$d_{\max} = -\frac{(m+1)V_{\max}}{2L}\ln(R), \tag{B-8}$$

where l denotes the distance from the calculation point to the inner absorbing boundary of the PML region, L is the thickness of the PML layer, m is the order of the polynomial, usually chosen as 2 or 3, and R is the theoretical reflection coefficient, set to 10^{-6} here. Moreover,

$$\chi_x = 1 + (\chi_{\max} - 1)\left(\frac{l}{L}\right)^m,$$
$$\alpha_x = \pi\alpha_{\max}\left(1 - \frac{l}{L}\right), \tag{B-9}$$

where $\chi_{\max}$ can be obtained by testing, $\alpha_{\max} = f_0$, and f_0 is the dominant frequency of the source wavelet.

Substituting these auxiliary variables into the velocity-stress-temperature equation 10, the final RSG-FD scheme with the CPML technique is equation 20.

APPENDIX C

PLANE-WAVE ANALYSIS

To show the characteristics of the wave propagation, we consider the plane waves

$$\mathbf{u} = \mathbf{U}\exp[i\omega(t - \mathbf{d}\cdot\mathbf{x})], \quad T = T_0\exp[i\omega(t - \mathbf{d}\cdot\mathbf{x})], \tag{C-1}$$

where ω denotes the angular frequency, t is the time, $\mathbf{d}$ is the slowness vector, $\mathbf{x}$ is the position vector, and $i = \sqrt{-1}$. The terms $\mathbf{U}$ and T_0 define the amplitude of displacement and temperature fields, respectively. In terms of the complex velocity V_c, $\mathbf{d}$ is written as $\mathbf{d} = \mathbf{N}/V_c$, where $\mathbf{N} = (n_1, n_2, n_3)$ denotes the direction of propagation. Substituting equation C-1 into equation 7, and assuming $U_i l_i = 0$ and $U_i l_i = 1$, yields two equations for the S- and P-waves, respectively. Hence, the phase velocity of the S-wave is

$$V_s = \sqrt{\mu/\rho}. \tag{C-2}$$

Because μ and ρ are not affected by the thermal properties in the homogeneous case, the S-wave is not affected by the temperature. The P-wave complex velocity is

$$V_c^2 = \frac{1}{2}\left[V_A^2 + M \pm \sqrt{(V_A^2 + M)^2 - 4MV_I^2}\right], \tag{C-3}$$

where the minus and plus signs correspond to the T-wave and E-wave, respectively, and

$$M = i\omega a^2/(1 + i\omega\tau),$$
$$V_I = \sqrt{(\lambda + 2\mu)/\rho},$$
$$V_A = \sqrt{V_I^2 + b^2}, \tag{C-4}$$

where M denotes a complex kernel corresponding to the Maxwell viscoelastic mechanical model (Carcione, 2014), V_A and V_I are the adiabatic and isothermal phase velocities, respectively, $b=\gamma\sqrt{T_0/(\rho c)}$, and $a = \sqrt{\kappa/c}$ is the thermal diffusivity. Thus, at $\omega = 0$, the solutions are

$$V_c = V_T = 0, V_c = V_E = V_A, \tag{C-5}$$

where V_T and V_E denote the velocities of the thermal wave (T-wave) and fast P-wave, respectively. For the lattice model, the relaxation time uses the relation $\tau = \kappa/(cV_I^2)$. Therefore, for $\omega \to \infty$, we have

$$2V_c^2 = V_A^2 + V_I^2 \pm \sqrt{(V_A^2 + V_I^2)^2 - 4V_I^4}. \tag{C-6}$$

Hence, the velocity approaches a finite value. The above complex velocities are used to compute the phase velocities V_p and attenuation factor A of the two longitudinal waves (Carcione et al., 2019b).

REFERENCES

Ackerman, C. C., B. Bertman, H. A. Fairbank, and R. A. Guyer, 1966, Second sound in solid helium: Physical Review Letters, **16**, 789–791, doi: 10.1103/PhysRevLett.16.789.

Biot, M. A., 1956a, Thermoelasticity and irreversible thermodynamics: Journal of Applied Physics, **27**, 240–253, doi: 10.1063/1.1722351.

Biot, M. A., 1956b, The theory of propagation of elastic waves in a fluid-saturated porous solid — 1: Low-frequency range — 2: Higher frequency range: The Journal of the Acoustical Society of America, **28**, 168–178, doi: 10.1121/1.1908239.

Boschi, E., 1973, A thermoviscoelastic model of the earthquake source mechanism: Journal of Geophysical Research, **78**, 7733–7737, doi: 10.1029/JB078i032p07733.

Carcione, J. M., 2014, Wave fields in real media: Theory and numerical simulation of wave propagation in anisotropic, anelastic, porous and electromagnetic media, 3rd ed.: Elsevier.

Carcione, J. M., F. Cavallini, E. Wang, J. Ba, and L. Y. Fu, 2019a, Physics and simulation of wave propagation in linear thermoporoelastic media: Journal of Geophysical Research, Solid Earth, **124**, 8147–8166, doi: 10.1029/2019JB017851.

Carcione, J. M., and G. Quiroga-Goode, 1995, Some aspects of the physics and numerical modeling of Biot compressional waves: Journal of Computational Acoustics, **3**, 261–280, doi: 10.1142/S0218396X95000136.

Carcione, J. M., Z. W. Wang, W. Ling, E. Salusti, J. Ba, and L. Y. Fu, 2019b, Simulation of wave propagation in linear thermoelastic media: Geophysics, **84**, no. 1, T1–T11, doi: 10.1190/geo2018-0448.1.

Chen, H., X. Wang, and H. Zhao, 2006, A rotated staggered grid finite-difference with the absorbing boundary condition of a perfectly matched layer: Chinese Science Bulletin, **51**, 2304–2314, doi: 10.1007/s11434-006-2127-8.

Deresiewicz, H., 1957, Plane waves in a thermoelastic solid: Journal of the Acoustical Society of America, **29**, 204–209, doi: 10.1121/1.1908832.

Faccioli, E., F. Maggio, R. Paolucci, and A. Quarteroni, 1997, 2D and 3D elastic wave propagation by a pseudo-spectral domain decomposition method: Journal of Seismology, **1**, 237–251, doi: 10.1023/A:1009758820546.

Fu, L. Y., 2012, Evaluation of sweet spot and geopressure in Xihu, Sag: Technical Report, CCL2012-SHPS-0018ADM, Key Laboratory of Petroleum Resource Research, Institute of Geology and Geophysics, Chinese Academy of Sciences.

Fu, L. Y., 2017, Deep-superdeep oil & gas geophysical exploration 111: Program report jointly initiated by MOE and SAFEA, B18055, School of Geosciences, China University of Petroleum (East China).

Fu, L. Y., and Y. G. Mou, 1994, Boundary element method for elastic wave forward modeling: Chinese Journal of Geophysics, **37**, 521–529.

Green, A. E., and K. A. Lindsay, 1972, Thermoelasticity: Journal of Elasticity, **2**, 1–7, doi: 10.1007/BF00045689.

Hu, S. Z., L. Y. Fu, and Z. L. Pei, 2009, A boundary element method for the 2D wave equation in fluid-saturated porous media: Chinese Journal of Geophysics, **52**, 2364–2369, doi: 10.3969/j.issn.0001-5733.2009.09.022.

Ignaczak, J., and M. Ostoja-Starzewski, 2010, Thermoelasticity with finite wave speeds: Oxford Science Publications.

Jackson, H. E., C. T. Walker, and T. F. McNelly, 1970, Second sound in NaF: Physical Review Letters, **25**, 26–28, doi: 10.1103/PhysRevLett.25.26.

Jacquey, A. B., M. Cacace, G. Blöcher, and M. Scheck-Wenderoth, 2015, Numerical investigation of thermoelastic effects on fault slip tendency during injection and production of geothermal fluids: Energy Procedia, **76**, 311–320, doi: 10.1016/j.egypro.2015.07.868.

Komatitsch, D., and R. Martin, 2007, An unsplit convolutional perfectly matched layer improved at grazing incidence for the seismic wave equation: Geophysics, **72**, no. 5, SM155–SM167, doi: 10.1190/1.2757586.

Lord, H. W., and Y. Shulman, 1967, A generalized dynamical theory of thermoelasticity: Journal of the Mechanics and Physics of Solids, **15**, 299–309, doi: 10.1016/0022-5096(67)90024-5.

Martin, R., and D. Komatitsch, 2009, An unsplit convolutional perfectly matched layer technique improved at grazing incidence for the viscoelastic wave equation: Geophysical Journal International, **179**, 333–344, doi: 10.1111/j.1365-246X.2009.04278.x.

McNelly, T. F., S. J. Rogers, D. J. Channin, R. J. Rollefson, W. M. Goubau, G. E. Schmidt, and R. O. Pohl, 1970, Heat pulses in NaF: Onset of second sound: Physical Review Letters, **24**, 100–102, doi: 10.1103/PhysRevLett.24.100.

Norris, A., 1992, On the correspondence between poroelasticity and thermoelasticity: Journal of Applied Physics, **71**, 1138–1141, doi: 10.1063/1.351278.

Rudgers, A. J., 1990, Analysis of thermoacoustic wave propagation in elastic media: The Journal of the Acoustical Society of America, **88**, 1078–1094, doi: 10.1121/1.399856.

Saenger, E. H., N. Gold, and S. A. Shapiro, 2000, Modeling the propagation of elastic waves using a modified finite-difference grid: Wave Motion, **31**, 77–92, doi: 10.1016/S0165-2125(99)00023-2.

Saenger, E. H., and S. A. Shapiro, 2002, Effective velocities in fractured media: A numerical study using the rotated staggered finite-difference grid: Geophysical Prospecting, **50**, 183–194, doi: 10.1046/j.1365-2478.2002.00309.x.

Serón, F. J., F. J. Sanz, M. Kindelan, and J. I. Badal, 1990, Finite-element method for elastic wave propagation: Communications in Applied Numerical Methods, **6**, 359–368, doi: 10.1002/cnm.1630060505.

Shaw, S., and B. Mukhopadhyay, 2011, Thermo elastic waves with thermal relaxation in isotropic micropolar plate: Sadhana, **36**, 209–221, doi: 10.1007/s12046-011-0015-7.

Veres, I. A., T. Berer, and P. Burgholzer, 2013, Numerical modeling of thermoelastic generation of ultrasound by laser irradiation in the coupled thermoelasticity: Ultrasonics, **53**, 141–149, doi: 10.1016/j.ultras.2012.05.001.

Virieux, J., 1986, P-SV wave propagation in heterogeneous media: Velocity-stress finite-difference method: Geophysics, **51**, 889–901, doi: 10.1190/1.1442147.

Wang, E., J. M. Carcione, J. Ba, M. Alajmi, and A. N. Qadrouh, 2019, Nearly perfectly matched layer absorber for viscoelastic wave equations: Geophysics, **84**, no. 5, T335–T345, doi: 10.1190/geo2018-0732.1.

Wang, Y. H., and J. C. Santamarina, 2007, Attenuation in sand: An exploratory study on the small-strain behavior and the influence of moisture condensation: Granular Matter, **9**, 365–376, doi: 10.1007/s10035-007-0050-6.

Wang, Z. W., L. Y. Fu, J. Wei, W. T. Hou, J. Ba, and J. M. Carcione, 2020, On the Green function of the Lord-Shulman thermoelasticity equations: Geophysical Journal International, **220**, 393–403, doi: 10.1093/gji/ggz453.

Wei, J., L. Y. Fu, Z. W. Wang, J. Ba, and J. M. Carcione, 2020, Green's function of the Lord-Shulman thermo-poroelasticity theory: Geophysical Journal International, **221**, 1765–1776, doi: 10.1093/gji/ggaa100.

Zhang, Y., L. Y. Fu, L. Zhang, W. Wei, and X. Guan, 2014, Finite difference modeling of ultrasonic propagation (coda waves) in digital porous cores with un-split convolutional PML and rotated staggered grid: Journal of Applied Geophysics, **104**, 75–89, doi: 10.1016/j.jappgeo.2014.02.012.

Biographies and photographs of the authors are not available.